PCCP

Accepted Manuscript

This is an *Accepted Manuscript*, which has been through the Royal Society of Chemistry peer review process and has been accepted for publication.

Accepted Manuscripts are published online shortly after acceptance, before technical editing, formatting and proof reading. Using this free service, authors can make their results available to the community, in citable form, before we publish the edited article. We will replace this *Accepted Manuscript* with the edited and formatted *Advance Article* as soon as it is available.

You can find more information about *Accepted Manuscripts* in the Information for Authors.

Please note that technical editing may introduce minor changes to the text and/or graphics, which may alter content. The journal's standard Terms & Conditions and the Ethical guidelines still apply. In no event shall the Royal Society of Chemistry be held responsible for any errors or omissions in this *Accepted Manuscript* or any consequences arising from the use of any information it contains.

ROYAL SOCIETY OF CHEMISTRY

www.rsc.org/pccp

Journal Name RSCPublishing

ARTICLE

Tuning the properties of visible-light-responsive tantalum (oxy)nitride photocatalysts by non-stoichiometric compositions: a first-principle viewpoint

Cite this: DOI: 10.1039/x0xx00000x

Received 00th January 2012,
Accepted 00th January 2012

DOI: 10.1039/x0xx00000x

www.rsc.org/

Moussab Harb,*[,a] Philippe Sautet,[b] Ela Nurlaela,[a] Pascal Raybaud,[c] Luigi Cavallo,[a] Kazunari Domen,[d] Jean-Marie Basset[a] and Kazuhiro Takanabe*[,a]

Finding an ideal photocatalyst for achieving efficient overall water splitting still remains a grant challenge. By applying accurate first-principle quantum calculations based on DFT with the screened non-local hybrid HSE06 functional, we bring rational insights at atomic level into the influence of non-stoichiometric compositions on essential properties of tantalum (oxy)nitride compounds as visible-light-responsive photocatalysts for water splitting. Indeed, recent experiments show that such non-stoichiometry is inherent to the nitridation methods of tantalum oxide with unavoidable oxygen impurities. We considered here O-enriched Ta_3N_5 and N-enriched TaON materials. Although their structural parameters are found to be very similar to those of pure compounds and in good agreement with available experimental works, their photocatalytic features for visible-light-driven overall water splitting reactions show different behaviors. Further partial nitration of TaON leads to a narrowed band gap, but partially oxidizing Ta_3N_5 causes only subtle changes in the gap. The main influence, however, is on the band edge positions relative to water redox potentials. The pure Ta_3N_5 is predicted to be a good candidate only for H^+ reduction and H_2 evolution, while the pure TaON is predicted to be a good candidate for water oxidation and O_2 evolution. Non-stoichiometry has here a positive influence, since partially oxidized tantalum nitride, $Ta_{(3-x)}N_{(5-5x)}O_{5x}$ (for $x \geq 0.16$) i.e. with a composition in between TaON and Ta_3N_5, reveals suitable band edge positions that correctly bracket the water redox potentials for visible-light-driven overall water splitting reactions. Among the various explored $Ta_{(3-x)}N_{(5-5x)}O_{5x}$ structures, a strong stabilization is obtained for the configuration displaying a strong interaction between the O-impurities and the created Ta-vacancies. In the lowest-energy structure, each created Ta-vacancy is surrounded by five O-impurity species substituting the five N sites characterizing one octahedral environment.

Introduction

Since the discovery of H_2 evolution through the photoelectrochemical decomposition of water on TiO_2 electrodes in 1972, semiconductor-based photocatalysis for water splitting has attracted a strong interest for the potential production of clean H_2 from water using solar energy.[1-4] To achieve efficient water splitting, two basic requirements need simultaneously to be satisfied for the semiconductor photocatalyst as a photon absorber: (i) the band gap should be adequate (greater than 1.23 eV) to absorb a wide range of the visible light (thermodynamically up to ~1000 nm), which accounts for 43 % of the solar energy spectrum; (ii) the valence band and conduction band edges should straddle the water oxidation (O_2/H_2O) and reduction (H^+/H_2) potentials to give electrons and holes that overcome kinetic overpotential to reduce H^+ and to oxidize water.

Transition metal oxides photocatalysts have been the subject of most previous studies[2, 5] for their good chemical stability in aqueous solution. However, their relatively large band gap ($\geq$ 3 eV) makes them efficient only under UV light, which accounts for only ~3 % of the solar to hydrogen energy efficiency. In contrast, transition metal nitrides usually have a smaller band gap than the corresponding oxides, but their easy oxidation in aqueous solution threatens to degrade them quickly.[2, 5, 6] The search for a new class of solid-state compounds exhibiting new physicochemical properties such as smaller band gaps than oxides and better chemical stability than nitrides has led to oxynitrides.[2, 5, 6] The properties of these compounds are known to be predominantly influenced by the amount of nitrogen incorporated into the oxide or of the oxygen amount introduced into the nitride.[7] This influence offers a great opportunity to achieve tunable or controllable properties by varying the oxygen:nitrogen ratio.[8-10]

In this context, tantalum oxynitride (TaON) and tantalum nitride (Ta_3N_5) have received a considerable attention over the past years for their suitable band gaps estimated at 2.5 and 2.1 eV, respectively.[10-13] Experimentally, TaON and Ta_3N_5 powders are generally produced through the high-temperature ammonolysis of amorphous or crystalline Ta_2O_5 under various temperature and heating time regimes.[12, 14-17] Characterizing the resulting samples through neutron and synchrotron powder diffraction analysis revealed monoclinic (known as β-phase) and orthorhombic crystal structures for TaON and Ta_3N_5, respectively.[12, 15, 18] It has been reported that both materials can generate H_2 or O_2 from water under visible light in the presence of sacrificial reagents.[12] Thus far, efficient overall water splitting has not been achieved using these photocatalysts. In addition, the band gap and photocatalytic activity of these materials were found to be dependent on the temperature, flow rate and duration of the nitridation process.[14, 15, 19] A suggested explanation of this phenomenon was related to the variation of the amount of O impurities remaining in Ta_3N_5.[15, 19] Our recent work confirmed that a significant amount of oxygen remains both in the bulk and on the surface of Ta_3N_5 samples.[20] This result was consistent with elemental microanalysis indicating that the Ta_3N_5 samples synthesized at high temperatures are non-stoichiometric or defective compounds and always contain a considerable amount of O impurities.[15, 19, 20] However, several non-stoichiometric chemical compositions were also proposed for the synthesized TaON samples with various O/N ratios.[15,20] Precise control of the stoichiometry and oxygen content in NH_3 nitridation is difficult to be achieved. Thus, the goal of the study presented herein is to provide a detailed understanding of the effects of chemical compositions on the photocatalytic features for water splitting of TaON- and Ta_3N_5-based materials that might be obtained from ammonolysis of Ta_2O_5 using advanced DFT calculations.

A few theoretical studies[18, 21-24] have been published on the electronic structure of TaON and Ta_3N_5, and a recent study[25] appeared on O-doped Ta_3N_5. Using the DFT-GGA approach, Fang et al.[21] initially calculated the density of states of TaON and Ta_3N_5 and they reported band gaps of 1.8 and 1.1 eV, respectively. In contrast, Stampfl et al.[22, 23] predicted a band gap of 1.5 eV for pure Ta_3N_5 using the DFT-LDA approach. Later, Yashima et al.[18] reported the DOS of TaON calculated using the DFT-PBE method with a band gap of 2.1 eV. Li et al.[24] showed a DOS of TaON calculated using the DFT-LDA method with a band gap of 1.92 eV. Although both the DFT-LDA and -GGA methods give very good structural results of semiconductors, they are well documented to strongly underestimate their band gaps,[26, 27] which are instead more accurately calculated using recent hybrid functionals such as HSE06.[27-31] To overcome the weaknesses of GGA functionals, Wang et al.[25] recently performed GGA+U calculations to study the effects of O doping on the photocatalytic properties of Ta_3N_5. By empirically varying the U values on Ta and N, they fitted the experimental band gap of Ta_3N_5 samples and calculated the DOS of O-doped Ta_3N_5 by considering only one substitutional O at N site into several Ta_3N_5 supercell sizes to simulate different levels of O impurities. In addition to the results obtained by Wang et al.,[25] several key aspects need to be further investigated to fully determine the effects of O impurities on the photocatalytic properties of Ta_3N_5 and obtain rational insights for improving the photocatalytic performance of this material. First, two other potential O-doped Ta_3N_5 structures that are associated with substitutional O species at N sites in the presence of Ta vacancies and substitutional O at N sites mixed with interstitial O have not been considered. Next, the UV-Vis optical absorption properties of O-doped Ta_3N_5 have not been explicitly simulated for each configuration to correctly interpret the available experimental data. Moreover, the band edges of pure Ta_3N_5 have not been calculated using an advanced SCF quantum method such as DFT-HSE06. Finally, the thermodynamic stability of the various TaON- and Ta_3N_5-based materials that might be obtained from ammonolysis of Ta_2O_5 as a function of the preparation conditions still remains unclear and needs to be clarified.

To address all the challenging questions invoked above, we start from recent structural data for these catalysts and report here a systematic and comprehensive theoretical study on the structural, electronic, optical, redox and energetic properties of tantalum (oxy)nitride compounds as visible-light-responsive photocatalysts obtained either from a partial oxidation of Ta_3N_5 or by a further nitridation of TaON. To ensure accurate band gap and optical transition predictions of these materials, we used advanced first-principles quantum calculations based on DFT and density functional perturbation theory (DFPT) within the screened non-local hybrid (HSE06) exchange-correlation formalism. First, we explored relevant N-enriched TaON structures by introducing various N species at O sites in the presence of additional O-vacancies. Also, we investigated two potential candidates of O-enriched Ta_3N_5 structures by incorporating various O species at N sites in the presence of Ta-vacancies or mixed with additional inserted O. Second, we calculated the electronic structure and UV-Vis optical absorption properties of the various explored materials. Third, we calculated their valence and conduction band edge positions relative to vacuum level (or to NHE potential) using an advanced first-principle quantum scheme described in the theoretical methods. Finally, we investigated the thermodynamics of the various explored materials under ammonia NH_3 as nitrogen source to mimic the protocol that is most commonly used to synthesize these materials.

Results and discussion

Structural characterization

The nitridation of tantalum oxide in NH_3 flow proceeds in a complex manner where the solid-state diffusion of anion replacements (N^{3-} vs. O^{2-}) occurs while gaseous NH_3 decomposes to nitrogen and hydrogen at high temperatures.[12, 47-51] The process of anion diffusion requires the substitution of three oxygen atoms with two nitrogen atoms to maintain a high oxidation state of the Ta d^0 electronic configuration (Ta^{5+}). As observed in SEM images of the samples (Figure S3), the process essentially creates the porous morphology of the nitrided products. The XRD patterns for the prepared Ta_2O_5, TaON, and Ta_3N_5 samples are shown in Figure S4. The successive nitridation completely changes the crystal structures of the products from the initial Ta_2O_5 to monoclinic TaON and thence to orthorhombic Ta_3N_5, which is consistent with the literature.[10-13] The introduction of H_2O into the NH_3 flow during nitridation successfully forms TaON instead of Ta_3N_5 under the same nitridation flow rate (200 mL min^{-1}), temperature (900 °C) and time (15 h) with no indication of an impurity phase in the XRD pattern, as discussed in greater detail below. Although XRD patterns show a pure phase, the formation of exact stoichiometry is not possible.[20] The lattice parameters obtained from the XRD measurements together are listed in Table 2 to provide the basis of the data.

Journal Name RSCPublishing

ARTICLE

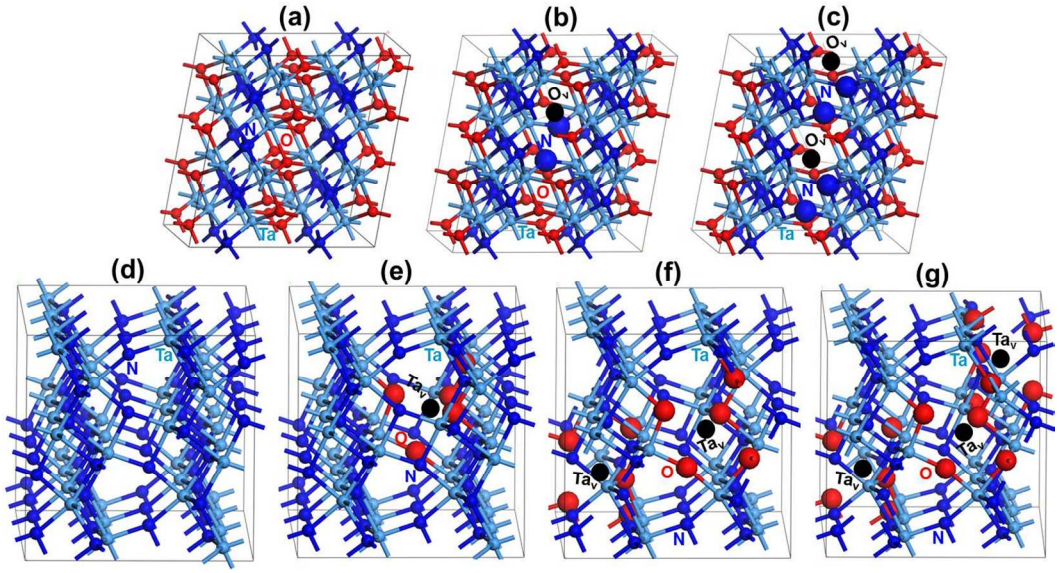

Figure 1. DFT-optimized lowest-energy structures obtained using the DFT-PBE method for: (a) TaON, (b) $TaO_{0.90}N_{1.06}$, (c) $TaO_{0.81}N_{1.12}$, (d) Ta_3N_5, (e) $Ta_{2.91}N_{4.58}O_{0.41}$, (f) $Ta_{2.83}N_{4.16}O_{0.83}$, and (g) $Ta_{2.75}N_{3.75}O_{1.25}$. Color legend: Ta in light blue, O in red, N in dark blue, O and Ta vacancies in black. The additional N substituting O sites in (b) and (c) are shown in big size balls.

Table 2. Calculated lattice parameters obtained using the DFT-PBE method for the various optimized structures reported in Figure 1. Comparison with the available experimental data.

stoichiometry	structure	lattice parameters					
		a (Å)	b (Å)	c (Å)	α (º)	β (º)	γ (º)
TaON	This work	4.96	5.02	5.17	90	99.8	90
TaON	Expt[18]	4.95	5.01	5.16	90	99.6	90
TaON	(1a)	4.97	5.03	5.18	90	99.7	90
$TaO_{0.90}N_{1.06}$	(1b)	4.97	5.04	5.18	90	99.8	90.1
$TaO_{0.81}N_{1.12}$	(1c)	4.98	5.04	5.18	90	99.9	89.5
Ta_3N_5	This work	3.89	10.22	10.27	90	90	90
Ta_3N_5	Expt[15]	3.89	10.22	10.28	90	90	90
Ta_3N_5	(1d)	3.89	10.25	10.27	90	90	90
$Ta_{2.91}N_{4.58}O_{0.41}$	(1e)	3.89	10.23	10.27	90	90	90
$Ta_{2.83}N_{4.16}O_{0.83}$	(1f)	3.89	10.20	10.26	90	90	90
$Ta_{2.75}N_{3.75}O_{1.25}$	(1g)	3.89	10.18	10.24	90	90	90

For the DFT calculation, the relative stability of the various explored materials is discussed here. The lowest-energy structures for the relevant materials are shown in Figure 1, while the corresponding lattice parameters are reported in Table 2. The metastable structures obtained for $TaO_{0.90}N_{1.06}$ and $Ta_{2.91}N_{4.58}O_{0.41}$ materials together with their relative energies are given in the Supplementary Information (Figure S5). The lowest-energy and metastable structures obtained for $Ta_3N_{4.83}O_{0.25}$ together with the calculated lattice parameters and relative energies are given in the Supplementary Information (Figure S6).

As shown in Table 2, our calculated lattice parameters for TaON and Ta_3N_5 are found in excellent agreement with the available experimental data.[15, 18] In TaON phase (Figure 1a),

the various bond lengths constituting one TaO_3N_4 polyhedral environment were found at 2.03/2.15 Å for Ta-O and 2.06/2.13 Å for Ta-N. In Ta_3N_5 phase (Figure 1d), Ta-N bond lengths of 2.0 and 2.23 Å were obtained for one TaN_6 octahedral environment.

If we discuss now the $TaO_{0.90}N_{1.06}$ material modeled by replacing two neutral O atoms by two N atoms and by removing one additional O atom from the 96-atom monoclinic TaON supercell, the lowest-energy structure configuration is obtained when these replacements and vacancy formation occur in a single TaO_3N_4 polyhedron, which leads to the formation of one TaN_6 octahedron, two TaO_2N_5 polyhedra and one $TaON_6$ polyhedron (Figure 1b) with new shorter Ta-N bond lengths of 1.96, 1.97 and 1.99 Å. In this structure, the two additional N are separated by 2.53 Å. The most stable spin configuration of this system is singlet, leading formally to two diamagnetic N^{3-} impurities substituting three O^{2-} species. The lattice parameters for this structure are very close to the values obtained for TaON (Table 2). Another structural configuration, with the two additional N separated by a longer distance of 4.70 Å, was found to be 0.28 eV (see Figure S5 for more details). A similar structural result is obtained for $TaO_{0.81}N_{1.12}$, in which the four N atoms substituting four O atoms and the removal of two additional O atoms occurred in two vicinal TaO_3N_4 polyhedra (Figure 1c).

Considering now the $Ta_{2.91}N_{4.58}O_{0.41}$ material simulated by replacing five neutral N atoms by five O atoms and by removing one Ta atom from the 96-atom orthorhombic Ta_3N_5 supercell, a strong stabilization is obtained for the configuration displaying a direct interaction between the five incorporated O and the created Ta-vacancy. In the lowest-energy structure, the five O preferentially occupy the five N sites surrounding the Ta-vacancy. These O species are disposed in one octahedral environment (Figure 1e) to form new shorter Ta-O bond lengths of 1.87, 1.98, 2.0, 2.07 and 2.22 Å. In this case as well, the optimized lattice parameters are very similar to those of pure Ta_3N_5 (Table 2). A singlet spin state is the most stable spin configuration for this structure, associated formally to five O^{2-} impurities substituting five N^{3-} species in conjunction with the creation of the Ta-vacancy. In contrast, another structural configuration displaying five O atoms and one Ta-vacancy, which are well separated from each other, was found 3.43 eV less stable (see Figure S5 for more details). Similar results are obtained for $Ta_{2.83}N_{4.16}O_{0.83}$ and $Ta_{2.75}N_{3.75}O_{1.25}$ materials, in which the structures are strongly stabilized when the ten and fifteen incorporated O occupied the ten and fifteen N sites surrounding two and three Ta-vacancies, respectively, as shown in Figure 1f, 1g. The relaxed lattice parameters for these structures are also found to be very similar to the values obtained for Ta_3N_5 (Table 2).

As a consequence, our calculations show remarkable similarities of lattice parameters between TaON and $TaO_{(1-3x)}N_{(1+2x)}$ materials as well as between Ta_3N_5 and $Ta_{(3-x)}N_{(5-5x)}O_{5x}$ materials. These results give an evidence of the possible presence in the experiments of these two particular non-stoichiometric oxynitride compounds together with the prefect materials.

Band gap engineering and UV-Vis optical absorption modification as a function of O/N and N/Ta ratios

Experimental band gaps for Ta_2O_5, TaON and Ta_3N_5 were determined from Tauc's plots of the DR UV-Vis spectra of the samples. The DR UV-Vis spectra and corresponding Tauc's plots are shown in Figure 2. Tauc's plots showed the measured band gaps for Ta_2O_5, TaON and Ta_3N_5 of 4.1, 2.8 and 2.1 eV for direct allowed transition and 3.9, 2.4 and 2.0 eV for indirect allowed transition, respectively.

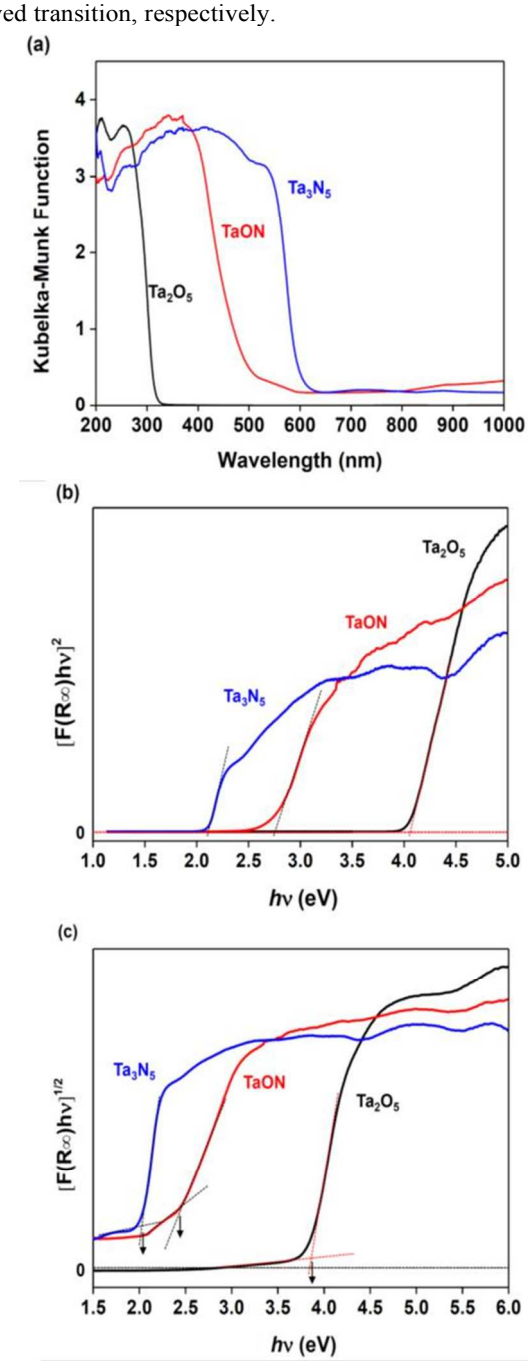

Figure 2. (a) Diffuse reflectance spectra, (b) Tauc's plot for direct band gap, and (c) Tauc's plot for indirect band gap for Ta_2O_5, TaON, and Ta_3N_5.

Journal Name RSCPublishing

ARTICLE

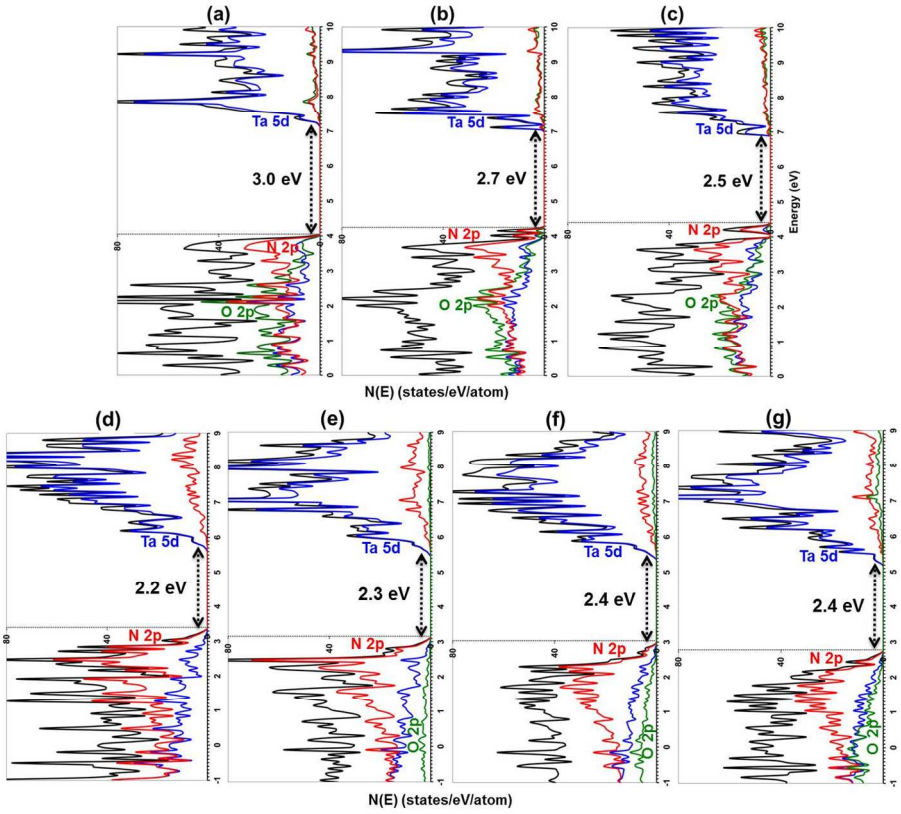

Figure 3. Calculated electronic density of states (DOS) using the DFT-HSE06 method for the optimized lowest-energy structures reported in Figure 1: (a) TaON; (b) $TaO_{0.90}N_{1.06}$; (c) $TaO_{0.81}N_{1.12}$; (d) Ta_3N_5; (e) $Ta_{2.91}N_{4.58}O_{0.41}$; (f) $Ta_{2.83}N_{4.16}O_{0.83}$; and (g) $Ta_{2.75}N_{3.75}O_{1.25}$. Color legend: total DOS in black, projected contributions from Ta 5d orbitals in blue, from O 2p orbitals in green, and from N 2p orbitals in red. The top of the valence bands are represented by the black dashed horizontal lines.

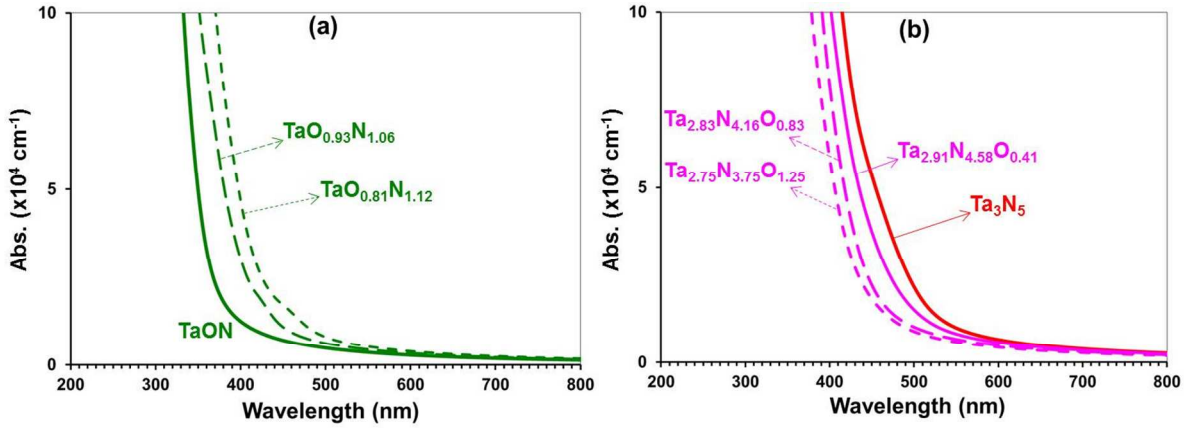

Figure 4. Calculated UV-Vis optical absorption coefficient spectra using the DFPT-HSE06 method for the various materials reported in Figure 3: (a) TaON, $TaO_{0.90}N_{1.06}$, and $TaO_{0.81}N_{1.12}$; (b) Ta_3N_5, $Ta_{2.91}N_{4.58}O_{0.41}$, $Ta_{2.83}N_{4.16}O_{0.83}$, and $Ta_{2.75}N_{3.75}O_{1.25}$.

Journal Name RSCPublishing

ARTICLE

For TaON, the density of states (DOS) calculated using the DFT-HSE06 method gives a band gap of 3.0 eV, as shown in Figure 3a. The electronic analysis reveals that the top part of the valence band (within 1.2 eV) is dominated by occupied N 2p states and that the lower part governed by occupied O 2p states, in clear relation with the different electronegativity of these two atoms. The conduction band is primarily composed of empty Ta 5d states. As a result of the predicted band gap, our UV-Vis optical absorption coefficient spectrum calculated using the DFPT-HSE06 method shows an absorption onset at 414 nm (Figure 4a). The density of states of TaON calculated using the DFT-PBE method revealed a much smaller band gap of 1.9 eV (see Figure S7 for more details), which is in agreement with the previous theoretical calculations.[18, 21, 24]

If we consider now the N-enriched TaON materials, the DOS analysis for $TaO_{0.90}N_{1.06}$ (O/N = 0.87) reveals a narrower band gap of 2.7 eV (Figure 3b) originating from the incorporation of new occupied electronic states on top of the original valence band of TaON. These new electronic states are predominantly composed of N 2p states with minor contributions from O 2p or Ta 5d states. A further decrease in the O/N ratio to 0.72, as in $TaO_{0.81}N_{1.12}$, slightly narrows the band gap to 2.5 eV (Figure 3c). Similar to $TaO_{0.90}N_{1.06}$, the top part of the valence band here is dominated by N 2p states. As a result of the band gap narrowing in these materials, the calculated UV-Vis optical absorption coefficient spectra are red-shifted over TaON, with an absorption edge extending up to 460 and 497 nm, respectively, as shown in Figure 4a. The lowest-energy band gaps in these two materials originate from N $2p^6$ - Ta $5d^0$ orbitals transitions. Interestingly, our calculated band gap value of 2.5 eV with HSE06 for $TaO_{0.81}N_{1.12}$ closely matches the available experimental data reported on the synthesized TaON samples.[12, 14, 17, 20] Moreover, the shape of the UV-Vis optical absorption edge of this material closely matches the observed experimental one.[12, 20] Considering the accuracy of band gap prediction using the HSE06 functional, this result indicates that the experimentally prepared tantalum oxynitride materials are not fully stoichiometric but slightly enriched in N, closer to $TaO_{0.81}N_{1.12}$ rather than TaON.

For pure Ta_3N_5, the density of states (DOS) calculated using the DFT-HSE06 method predicts a band gap of 2.2 eV, as shown in Figure 3d. The electronic analysis reveals a valence band governed by occupied N 2p states and a conduction band primarily composed of empty Ta 5d states. As expected, our band gap of 2.2 eV calculated using HSE06 matches very well the available experimental data reported on the synthesized Ta_3N_5 samples.[12, 15-17, 20] Based on the DOS result, our UV-Vis optical absorption coefficient spectrum calculated using the DFPT-HSE06 method reveals a broad absorption edge extending up to 564 nm, as shown in Figure 4b. The lowest-energy band gap in this compound involves transitions between N $2p^6$ orbitals and Ta $5d^0$ orbitals. We have also calculated the DOS of this material using the DFT-PBE method, and again, a much smaller band gap of 1.2 eV was obtained (see Figure S7 for more details), similar to the results reported in previous theoretical works.[21-23] This result confirms once again the crucial need of using HSE06 functional for obtaining accurate band gap values.

Considering now the O-enriched Ta_3N_5 materials, the DOS analysis for $Ta_{2.91}N_{4.58}O_{0.41}$ (O/N = 0.09) shows a slightly broader band gap of 2.3 eV (Figure 3e). A further increase in the O/N ratio to 0.2 or 0.33, as in $Ta_{2.83}N_{4.16}O_{0.83}$ or $Ta_{2.75}N_{3.75}O_{1.25}$, only marginally affects the band gap, with a slight increase to 2.4 eV (Figure 3f, 3g). Similar to pure Ta_3N_5, the top part of the valence band in these four compounds is dominated by occupied N 2p states due to the very weak contributions from O 2p states distributed over a wide energy range in the deeper part of the valence band. As a result of the small band gap broadening in these three last materials, their calculated UV-Vis optical absorption coefficient spectra are found to be slightly blue-shifted over pure Ta_3N_5, revealing new absorption onsets at 540, 517 and 497 nm, respectively (Figure 4b). For $Ta_3N_{4.83}O_{0.25}$ (O/N = 0.051 and N/Ta = 1.61), a very similar band gap and UV-Vis optical absorption response were obtained to the values for pure Ta_3N_5. The results are shown in Figure S8. Similar to pure Ta_3N_5, the lowest-energy band gaps in these three semiconducting compounds involve transitions between N $2p^6$ orbitals and Ta $5d^0$ orbitals. Contrasting with the previous cases of N-enriched TaON materials, the band gap of Ta_3N_5 is slightly affected by the presence of such O impurities in the lattice. The difference here is mainly due to the lower electronegativity of O versus N which generates new O 2p impurity states that are located lower in energy than the N 2p states. Although the electronic structures of O-enriched Ta_3N_5 semiconducting materials are similar to pure Ta_3N_5, their photocatalytic activity could be different based on the modifications in their band edge positions relative to water redox potentials. This aspect is discussed in detail below.

Band edge positions modification as a function of O/N and N/Ta ratios

In the water splitting reaction, the photocatalytic ability of a semiconductor to undergo photoinduced electron/hole transfer to adsorbed species on its surface is driven by the valence and conduction band edge positions relative to water redox potentials. Thermodynamically, the band edge positions must bracket the water redox potentials: the valence band edge position (where the holes are positioned) must be more positive than O_2/H_2O potential for the hole to be able to oxidize water, and similarly, the conduction band edge position of the semiconductor (where the excited electrons are accommodated) must be more negative than H^+/H_2 potential for the electron to be able to reduce H^+.[52] Here, we discuss and evaluate the photocatalytic behaviors of the various explored materials discussed above based on their calculated valence and conduction band edge positions relative to water redox potentials.

The flat band potentials of TaON and Ta_3N_5 were experimentally estimated by the Mott-Schottky plots obtained from electrochemical impedance spectroscopy measurements. The Mott-Schottky plots, together with the results of cyclic

voltammograms (CVs), are shown in Figure S9. From the CVs, the appropriate potential range was selected to extract a double-layer capacitance region without Faradaic currents (typically 0.6 - 1.0 V vs. NHE). The Mott-Schottky analyses at pH 13.5 give typical n-type semiconductor characters and flat band potentials of ~ −0.5 V vs. NHE for both samples that were considered to be located close to their conduction band. Here, we assume that the band positions follow a typical pH dependence relationship of 0.059 × pH (in V), so that the band positions relative to water redox potentials remain constant at any pH. Knowing the measured band gap, the conduction and valence band positions were located at ~ -0.5 and ~ 2.3 V vs. NHE for TaON and at ~ -0.5 and ~ 1.6 V vs. NHE (at pH 0). These band positions are consistent with the literature.[13, 53] Among them, Chun et al. reported the Fermi levels to be close to 0 V vs. NHE for both TaON and Ta_3N_5 estimated by Ultraviolet Photoelectron spectroscopy (UPS) and the Mott-Schottky analyses on nitride grown on Ta metal substrate.[13] In our previous paper, however, the flat band potentials of the Ta_3N_5 samples were strongly influenced by the surface states and most likely by dopant effects such as O impurities remaining in the structure.[20] Keeping also in mind that the fabrication of suitable electrodes using powder samples is very difficult to be achieved,[13] we precisely address here the expected effects of chemical compositions on the band edge positions of TaON and Ta_3N_5 photocatalysts using accurate first-principle quantum calculations based on DFT with the screened non-local hybrid HSE06 functional.

For TaON and pure Ta_3N_5 materials, the calculated valence and conduction band edge positions relative to the vacuum level were obtained through equations (1) and (2) (see Figures S1 and S2 for more details). The band edge positions of O- or N-enriched materials were deduced from the DOS plots (Figure 3) according to their positions relative to the pure materials. Our results obtained using the DFT-HSE06 method, are displayed in Figure 5.

Discussing first the pure and O-enriched Ta_3N_5 materials, Figure 5 shows a remarkable trend, revealing a linear decrease in both the valence and conduction edge positions toward more positive values with increasing O/N ratio. For pure Ta_3N_5, it is important to stress that our HSE06 calculations predict the valence band edge position to be 0.3 eV more negative than the O_2/H_2O potential. The conduction band edge position is found to be 1.3 eV more negative than the H^+/H_2 potential. Because of its unsuitable valence band edge position with respect to the O_2/H_2O potential, the pure Ta_3N_5 material is predicted by HSE06 to be a good candidate only for H^+ reduction and H_2 evolution reaction. It is important to discuss here such possible error bars in the calculation of band edge positions. General benchmarks are available for the ionization potential and electron affinities of molecular set, and they indicate a mean absolute error of ~0.2 eV. In any case, however, the valence band edge position is not below the O_2/H_2O level, and so, the holes created upon photon absorption in pure Ta_3N_5 will have a very limited (if not null) capability to oxidize water. Additionally, the pH value is able to slightly affect the O_2/H_2O potential. In contrast, the position of the conduction band edge position is undoubtedly above the H^+/H_2 level, and the excited electrons thus have a strong capability to reduce H^+. To the best of our knowledge, this result has never been invoked in previous theoretical studies. Another important result is that the partial oxidation of Ta_3N_5, with successive O/N ratios of 0.09, 0.2 and 0.33, produces a progressive downward shift of the valence band edge position (by 0.2 eV for each step), thereby markedly enhancing its capability of oxidizing water and evolving O_2. Hence, the partial oxidation of Ta_3N_5, even if it does not modify significantly the band gap, has a strong positive influence on the photocatalytic properties. The inevitable oxidation in water, if it remains partial, should hence not be considered as a threat to the material but instead as an opportunity to improve the intrinsically low water oxidation capability of pure Ta_3N_5. The partial oxidation of Ta_3N_5 also downward shifts the conduction band edge position, but this shift does not compromise the net reducing capability of the photo-generated electrons. For a very low oxidation level of O/N = 0.05, as in $Ta_3N_{4.83}O_{0.25}$, both the valence and conduction band edge positions were found to be slightly shifted upward by 0.1 eV as compared with pure Ta_3N_5. The results are shown in the Supplementary Information (Figure S10). Interestingly, our predicted band edge positions for O-enriched Ta_3N_5 materials, in particular for the the non-stoichiometric $Ta_{(3-x)}N_{(5-5x)}O_{5x}$ (for $x \geq 0.16$) compounds, closely match the available experimental data reported on the synthesized Ta_3N_5 samples.[13, 20, 53] Considering the accuracy of band gap prediction using the HSE06 functional, this result confirms that the experimentally prepared tantalum nitride materials are not stoichiometric but strongly enriched in O, closer to $Ta_{(3-x)}N_{(5-5x)}O_{5x}$ (for $x \geq 0.16$) rather than Ta_3N_5.

Considering now the pure and N-enriched TaON materials, the band edge positions are completely different from the previous cases (Figure 5), and consequently, different photocatalytic behavior is expected. For TaON, it is important to stress that our HSE06 calculations predict the conduction band edge position to be 0.3 eV more positive than the H^+/H_2 potential and the valence band edge position to be 2.0 eV more positive than the O_2/H_2O potential. Thus, the TaON material is predicted by HSE06 to be a good candidate only for water oxidation and O_2 evolution reaction because of its unsuitable conduction band edge position with respect to the H^+/H_2 potential. Even if this value is tempered by considering the error bars in the orbital energy positions, the excited electrons to the conduction band of TaON upon photon absorption will have a very limited capability to reduce H^+. To the best of our knowledge, this result has never been invoked in previous theoretical studies. Decreasing the O/N ratio to 0.87 or 0.72, as in $TaO_{0.93}N_{1.06}$ or $TaO_{0.81}N_{1.12}$, further downward shifts the conduction band edge by 0.1 or 0.2 eV over TaON, respectively (e.g., they become 0.4 and 0.5 eV more positive than the H^+/H_2 potential).), hence lowering its capability of reducing H^+ and evolving H_2. In contrast, their respective valence band edge position is moved upward by 0.2 and 0.3 eV with respect to TaON (e.g., they become 1.8 and 1.7 eV more positive than the O_2/H_2O potential), and therefore, their power to oxidize water is maintained.

As a consequence, our HSE06 calculations clearly show that the further nitridation of TaON lowers its thermodynamic ability for H^+ reduction and H_2 evolution, while the partial oxidation of Ta_3N_5 greatly enhances its power for water oxidation and O_2 evolution. To the best of our knowledge, these significant effects of N or O impurities on the photocatalytic performance of TaON or Ta_3N_5 materials for overall water splitting reactions have never been reported in previous theoretical studies.

Journal Name RSCPublishing

ARTICLE

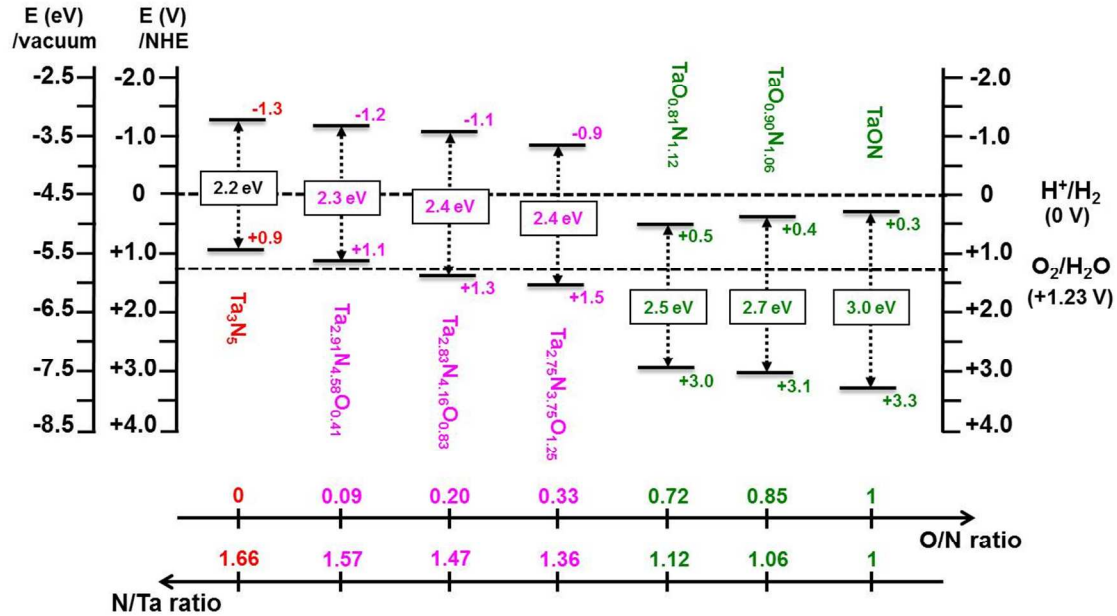

Figure 5. Calculated valence and conduction band edge positions of the various explored materials using the DFT-HSE06 method. The values are given with respect to the vacuum level (in eV) as well as with respect to the NHE potential (in V). The two black dashed horizontal lines represent the water redox potentials.

Thermodynamic stability of solids as a function of the water partial pressure

The thermodynamic stability of the various explored materials under NH_3 in the gas phase is investigated here. To mimic the most commonly used synthetic protocol, we fixed the chemical potential of ammonia, $\Delta\mu_{NH_3}$, at $p(NH_3)$ = 1 atm (standard thermodynamic conditions) and used a nitridation temperature of T = 1200 K (typical experimental annealing temperature for Ta_3N_5 material). The thermodynamic diagram is built by plotting the bulk formation energies of these materials as a function of the thermal part of the oxygen chemical potential, $\Delta\mu_O$, which is an important parameter characterizing the oxygen environment during synthesis. The environment acts as a reservoir, which can give or take any amount of oxygen without changing its temperature and pressure.[54, 55] Low or high values of $\Delta\mu_O$ correspond to O-poor or O-rich growth conditions. The range of $\Delta\mu_O$ is fixed by the partial pressure of water $p(H_2O)$ through equations (7) and (8) for T = 1200 K. The reference formation energy expressed for a unit containing 1 Ta atom corresponds to pure TaON. Lower or higher formation energies thus represent materials that are more or less stable than TaON.

Figure 6 shows the diagram for the formation energy of all of the compounds considered in this paper, namely, N-enriched TaON and O-enriched Ta_3N_5 (reactions (3), (4) and (5) and equations (6), (9) and (10)) for a fixed $\Delta\mu_{NH_3}$ = -1.81 eV at $p(NH_3)$ = 1 atm and T = 1200 K. Clearly, only a part of the $p(H_2O)$ range is accessible experimentally. A clear interval of stability for TaON is found for $p(H_2O)$ in between 10^{-1} and 1 atm. Above is the domain of Ta oxide Ta_2O_5, and below for a large range of $\Delta\mu_O$ corresponding to $p(H_2O) < 10^{-1}$ atm, is the domain of the Ta nitride Ta_3N_5. Although the partially oxidized Ta_3N_5 materials such as $Ta_3N_{4.83}O_{0.25}$, $Ta_{2.91}N_{4.58}O_{0.41}$, $Ta_{2.83}N_{4.16}O_{0.83}$ and $Ta_{2.75}N_{3.75}O_{1.25}$ are more stable than TaON for this large range of $\Delta\mu_O$ ($p(H_2O) < 10^{-1}$ atm), they remain slightly metastable with respect to pure Ta_3N_5 by +0.1-0.2 eV in the interval 10^{-3} atm < $p(H_2O)$ < 10^{-1} atm . The N-enriched TaON materials such as $TaO_{0.90}N_{1.06}$ and $TaO_{0.81}N_{1.12}$, become more stable than TaON only for highly reductive conditions and ultra low $p(H_2O)$ ($p(H_2O) < 10^{-4}$ atm) and that they remain highly metastable with respect to pure Ta_3N_5. In addition, the stability range of the oxynitride TaON phase is narrow between the oxide and the nitride. This result clearly explains the experimental difficulties in synthesizing this material.

As described in the thermodynamic calculation on the Ta-O-N system (Figure 6), we have experimentally demonstrated that selective control of the oxynitride phase (TaON) or nitride phase (Ta_3N_5) is achievable with or without introducing appropriate H_2O vapor in the NH_3 stream. This result is consistent with the previous literature,[14] where TaON synthesis is attempted with a humidified ammonia flow. The nitridation process is known to proceed via the successive transformation

of Ta_2O_5 → TaON → Ta_3N_5,[10-12] where a continuous dehydration reaction occurs. In our experiments, the water addition to NH_3 flow (0.03 atm H_2O) successfully changes the final form of nitridation product to TaON, whereas synthesis with dry NH_3 leads to Ta_3N_5. The thermodynamic stability diagram predicted by DFT calculation, as shown in Figure 6, provides a guideline for the experimentalists to optimize the preparation conditions under NH_3. Furthermore, this type of thermodynamic calculation has a high potential to be applicable in the prediction of the stability of various non-oxide materials, such as nitride, sulfide and carbides, starting from the oxide precursors.

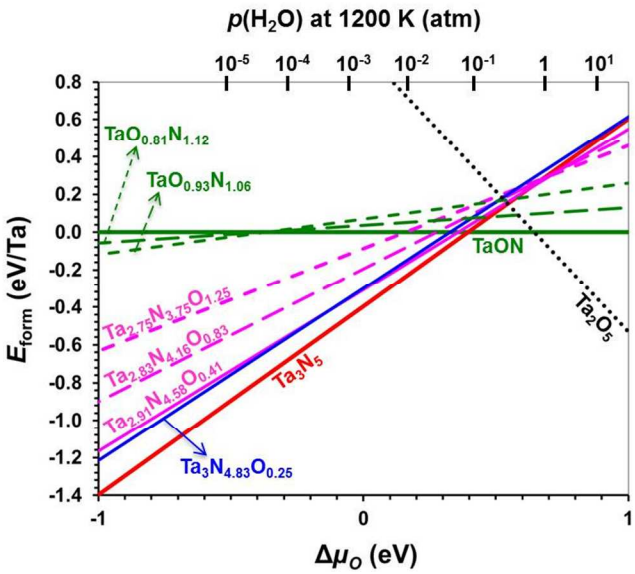

Figure 6. Calculated thermodynamic stability diagram for the various explored semiconducting materials as a function of the oxygen chemical potential $\Delta\mu_O$ and $p(H_2O)$ using NH_3 in gas phase for $\Delta\mu_{NH_3} = -1.81$ eV ($p(NH_3)$ = 1 atm; T = 1200 K). The black dashed lines represent Ta_2O_5 obtained from this reaction: $2TaON + 3H_2O \rightarrow Ta_2O_5 + 2NH_3$.

Conclusions

Using accurate first-principle quantum calculations based on DFT and density functional perturbation theory (DFPT) within the screened non-local hybrid HSE06 exchange-correlation functional, we obtained rational insights at atomic level into the influence of non-stoichiometric compositions on essential properties of tantalum (oxy)nitride compounds as visible-light-responsive photocatalysts for water splitting. We considered here O-enriched Ta_3N_5 and N-enriched TaON materials, based on experimental works[14, 15, 19, 20] showing that such non-stoichiometry is inherent to the nitridation method of tantalum oxide with unavoidable O impurities. Although their structural parameters were found to be very similar to those of pure compounds, their photocatalytic features for overall water splitting reactions showed different behaviors. The further partial nitration of TaON led to an important narrowing of the band gap but little band gap broadening was obtained when Ta_3N_5 was partially oxidized.

On the basis of calculated band edge positions relative to water redox potentials, we showed that pure Ta_3N_5 (calculated band gap of 2.2 eV) presents a good potential for H^+ reduction and H_2 evolution, but the holes created upon absorption are thermodynamically incapable of oxidizing water because the valence band edge position of this material was predicted to be 0.3 eV more negative than the O_2/H_2O potential. The partial oxidation of Ta_3N_5 led to a downward shift of the valence band edge, thereby enhancing its capability for water oxidation and towards O_2 evolution. In contrast, the conduction band edge position of TaON (calculated band gap of 3.0 eV) was predicted to be 0.3 eV more positive than the H^+/H_2 potential, and consequently, the excited electrons upon photon absorption are thermodynamically incapable of reducing H^+. The further partial nitration of TaON was unable to increase its capability for H^+ reduction and towards H_2 evolution. Only the non-stoichiometric $Ta_{(3-x)}N_{(5-5x)}O_{5x}$ (for $x \geq 0.16$) compounds, being in between TaON and Ta_3N_5, revealed suitable band edge positions for visible-light-driven overall water splitting similarly as it is experimental reported on the synthesized (oxy)nitride powders.[13, 20, 53] Our results hence suggest that non-stoichiometry and O impurities in the Ta_3N_5 material, which are clearly evidenced from experimental characterization, are keys for its successful activity as photocatalyst for water splitting. Reaching an optimal partial oxidation level of Ta3N5 should hence be targeted in the experiments. Among the various explored $Ta_{(3-x)}N_{(5-5x)}O_{5x}$ structures, a strong stabilization is obtained for the configuration displaying a strong interaction between the O impurities and the created Ta-vacancies. In the lowest-energy structure, each created Ta-vacancy is surrounded by five O-impurity species substituting the five N sites characterizing one octahedral environment. As a typical example, $Ta_{2.75}N_{3.75}O_{1.25}$ (x = 0.25 or O/N = 0.33 and N/Ta = 1.36) with a calculated band gap of 2.4 eV and a broad light absorption edge extending up to 520 nm, was found to be a suitable photocatalyst for both water oxidation and H^+ reduction. The valence band edge position of this material was predicted to be 0.3 eV more positive than the O_2/H_2O potential, and the conduction band edge position was 0.9 eV more negative than the H^+/H_2 potential.

In conclusion, we have demonstrated significant effects of non-stoichiometric compositions on relevant properties to solar water splitting using tantalum (oxy)nitride compounds as visible-light-responsive photocatalysts. The advanced first-principle quantum methodology described in this study can definitely be applied to identify good candidate photocatalysts among novel semiconducting compounds for visible-light-driven overall water splitting reactions.

Experimental and Theoretical Methods

Synthesis and characterization of TaON and Ta_3N_5

TaON and Ta_3N_5 particles were prepared from as-purchased commercially available crystalline Ta_2O_5 (≥99.99% metal basis, <5 microns, Sigma–Aldrich) by applying direct NH_3 nitridation under high temperature. A total of 0.5 g Ta_2O_5 was wrapped with quartz wool and placed in a tube furnace. The tube furnace was initially purged with N_2 prior to the introduction of NH_3 flow at room temperature. The nitridation was conducted at 900 °C, with a heating rate of 5 °C min^{-1}, and was held at this temperature for 15 h under a NH_3 flow of 200 mL min^{-1}. To selectively prepare the TaON phase, the same flow of NH_3 gas but with H_2O vapor (~0.03 atm) was used with a water saturator. The sample was allowed to cool to room temperature inside a tube furnace under NH_3 flow.

The morphology of the prepared particles was analyzed by scanning electron microscopy (SEM) performed on Nova Nano 630 at 5 kV voltage. The samples were prepared by simply

drop-casting ethanol dispersions of samples onto the SEM sample holder and naturally drying them before the analysis.

X-ray diffraction (XRD) patterns were collected on a Bruker D8 Advanced A25 diffractometer in the Bragg–Brentano geometry equipped with a Cu tube (Cu–Kα; λ = 0.15418 nm) operating at 40 kV and 40 mA using a linear position sensitive detector (opening 2.9°). The diffractometer was configured with a 0.44° diverging slit, 2.9° anti-scattering slit, 2.5° Soller slits, and a nickel filter to attenuate the contributions from Cu–Kβ fluorescence. Data sets were acquired in continuous scanning mode (0.004998°/s) over the 2θ range of 10–120°. The integration step size of 0.010° resulted in a counting time of 2 s per step.

The optical properties of the prepared samples were studied by diffuse-reflectance ultraviolet-visible (DR–UV–Vis) spectroscopy that was performed using a JASCO model V-670 spectrophotometer equipped with an integrating sphere. The spectra were scanned from 1000 to 200 nm using halogen and deuterium lamps as the light sources. Contributions from scattering were removed using the Kubelka–Munk function. The spectra were referenced to a Spectralon standard (Labsphere, Inc.), which reflects >99% of light in the 250-2000 nm range. The Kubelka-Munk function, $F(R_\infty)$ was determined from the UV-Vis absorbance, and the bandgap energy (E_g) was determined by finding the intercept of the straight line in the low-energy region of a plot of $[F(R\infty)h\nu]^n$, where n = 2 and 0.5 for the direct and indirect allowed transitions, respectively, vs. hν, where hν is the energy of the incident photons.

Electrochemical impedance spectroscopy was performed to estimate the flat-band potential and band positions of the prepared samples. For this purpose, the TaON and chemically etched Ta_3N_5 electrodes were fabricated using the electrophoretic deposition method.[20] One hundred milligrams of I_2 was dissolved in 25 mL of acetone, and 20 V was applied for 3 min to electrophoretically deposit the samples. The selected substrate was fluorine-doped tin oxide, which was dipped in the suspension to prepare a coated area of 2.0 × 1.0 cm^2. The counter electrode was another fluorine-doped tin oxide electrode that faced the previous electrode at a distance of 1 cm. The electrodes were then washed several times with acetone to remove the adsorbed iodine and were simply treated in a flow of NH_3 at 500 °C for 30 min before analysis. The electrolyte used for the electrochemical impedance spectroscopic investigations was a 1 M NaOH solution (pH = 13.5). The measurements were performed using a research-grade potentiostat system (VMP3) from BioLogic Science Instruments in a conventional three-electrode single electrochemical cell. An Ag/AgCl electrode and a carbon rod were used as the reference electrode and counter electrode, respectively. Prior to impedance spectroscopy, cyclic voltammetry experiments were conducted under Ar with a 50 mV s^{-1} scan rate between −0.5 and 1.8 V vs. NHE to determine the potential window for the Mott-Schottky analysis. Impedance spectra were then recorded between 10 Hz and 200 kHz under bubbling Ar, and the amplitude of the superimposed sinusoidal potential signal was 5 mV for each of the 70 steps in the potential window starting from 1.5 to 0 V vs. NHE.

Supercell models and structure optimization calculation

To simulate bulk N-enriched TaON and O-enriched Ta_3N_5 structures, we considered the (2 × 2 × 2) monoclinic TaON supercell and the (3 × 1 × 1) orthorhombic Ta_3N_5 supercell models, that contain 32 TaON units (or 96 atoms) and 12 Ta_3N_5 units (or 96 atoms), respectively. For N-enriched TaON, two or four substitutional N at O sites in the presence of one or two additional O-vacancies (labeled by $2N_s@O+1O_v$ and $4N_s@O+2O_v$) were considered. For O-enriched Ta_3N_5, five, ten or fifteen substitutional O at N sites coupled with one, two or three Ta-vacancies (labeled by $5O_s@N+1Ta_v$, $10O_s@N+2Ta_v$ and $15O_s@N+3Ta_v$) as well as two substitutional O at N sites mixed coupled with one additional interstitial O (labeled by $2O_s@N+1O_i$) were explored. Table 1 shows the various materials explored together with the corresponding stoichiometries. The overall supercell models remain neutral, whereas the presence of O- or N-impurity center induces local charge redistributions. In the $2N_s@O+1V_O$ model, N species are formally N^{3-}, while in the $2O_s@N+1O_i$ or $5O_s@N+1V_{Ta}$ models, O^{2-} species are created.

Table 1. Supercell models and stoichiometries (including *x*, *m*, *p*, and *k* values) for the various explored structures of N-enriched TaON and O-enriched Ta_3N_5 materials.

structure (system)	supercell model	stoichiometry	*x*	O/N	N/Ta
$2N_s@O+1O_v$ (TaON)	β-$Ta_nO_{(n-m)}N_{(n+p)}$ n=32; m=3; p=2	$TaO_{(1-3x)}N_{(1+2x)}$	0.03	0.85	1.06
$4N_s@O+2O_v$ (TaON)	β-$Ta_nO_{(n-m)}N_{(n+p)}$ n=32; m=6; p=4	$TaO_{(1-3x)}N_{(1+2x)}$	0.06	0.72	1.12
$2O_s@N+1O_i$ (Ta_3N_5)	$Ta_{3n}N_{(5n-p)}O_m$ n=12; p=2, m=3	$Ta_3N_{(5-2x)}O_{3x}$	0.08	0.05	1.61
$5O_s@N+1Ta_v$ (Ta_3N_5)	$Ta_{(3n-k)}N_{(5n-p)}O_m$ n=12; k=1; m=p=5	$Ta_{(3-x)}N_{(5-5x)}O_{5x}$	0.08	0.09	1.57
$10O_s@N+2Ta_v$ (Ta_3N_5)	$Ta_{(3n-k)}N_{(5n-p)}O_m$ n=12; k=2; m=p=10	$Ta_{(3-x)}N_{(5-5x)}O_{5x}$	0.16	0.20	1.47
$15O_s@N+3Ta_v$ (Ta_3N_5)	$Ta_{(3n-k)}N_{(5n-p)}O_m$ n=12; k=3; m=p=15	$Ta_{(3-x)}N_{(5-5x)}O_{5x}$	0.25	0.33	1.36

The various structures were optimized using DFT implemented in VASP5.2[32-35] within the PBE exchange-correlation functional[36] and the Projector-Augmented Plane Wave (PAW) approach.[37] Cutoff energies of 400 eV and 605.4 eV were used

for wave functions and for charge augmentations, respectively. The Brillouin zones were sampled with 3 × 3 × 3 Monkhorst-Pack *k*-point grid[38] for both supercell models. A convergence test made on both supercells with 5 × 5 × 5 *k*-point mesh revealed that the energy does not change more than 0.02 meV per TaON or Ta_3N_5 unit. The convergence criterion for the electronic self-consistent cycles was fixed at 10^{-5} eV per cell. The atomic coordinates and cell parameters were fully optimized until the values of all the residual forces components were less than 0.01 eV/Å.

Electronic structure and UV-Vis optical absorption calculations

To investigate the electronic density of states (DOS) of the materials, we employed the screened non-local hybrid HSE06 exchange-correlation functional,[39] as implemented in VASP 5.2,[32-35] based on the relaxed geometries obtained at PBE level. The tetrahedron method with Bloch corrections was used for the Brillouin zone integration. The choice of the HSE06 functional was based on our recent works on reference systems,[27-31] showing the high accuracy of this functional in predicting the experimental band gap of semiconductors.

To simulate the UV-Vis optical absorption properties of the materials, we applied the density functional perturbation theory (DFPT), as implemented in VASP5.2[32-35] by employing the HSE06 functional.[39] To determine the fraction of the light absorbed by these solids, we calculated the optical absorption coefficient (in cm^{-1}) of each compound as a function of the wavelength of the incident light using the equation $\alpha(\omega)=\frac{4\pi}{\lambda}k(\omega)$, where λ and ω are the wavelength and the frequency of the incident light, respectively, and $k(\omega)$ is the imaginary component of the complex refractive index or the extinction coefficient, which is defined by the following expression: $k(\omega)=\left(\frac{\sqrt{\varepsilon_1^2+\varepsilon_2^2}-\varepsilon_1}{2}\right)^{\frac{1}{2}}$.[40-42] $\varepsilon_1(\omega)$ and $\varepsilon_2(\omega)$ represent the real and imaginary parts, respectively, of the frequency-dependent complex dielectric function. The real part was calculated using the Kramers-Kronig relation while the imaginary part was calculated by summing all the possible transitions from occupied to unoccupied states in the Brillouin zone weighted with the matrix element describing the probability of transition. As a result of the accurate band gap determination provided by HSE06, the use of the DFPT-HSE06 approach is expected to accurately describe the optical transitions in semiconductors.[27-31]

Band edge positions calculation

To calculate the band edge positions of the semiconductor, the electronic band structure needs energetically to be aligned on a common energy scale. This can be accomplished by explicitly modelling a semiconductor-vacuum interface, which provides a vacuum reference for the electrostatic potential.[43, 44] The procedure consists of two separate calculations: (i) a first slab calculation to obtain the bulk band structure relative to the average electrostatic potential and (ii) a second slab calculation from which the alignment of the electrostatic potential within the material with respect to the vacuum level can be obtained. The valence and conduction band edge positions of TaON and Ta_3N_5 semiconductors relative to the vacuum level, denoted by E_{VB} and E_{CB}, respectively, were defined as follows:

$$E_{VB}=E_{VB}^{slab}-E_{VAC} \quad (1)$$

$$E_{CB}=E_{CB}^{slab}-E_{VAC} \quad (2)$$

where E_{VB}^{slab} and E_{CB}^{slab} are the energies of the valence and conduction band edges and E_{VAC} is the energy of the vacuum level obtained using the slab calculation. Hence, (1) and (2) shift the vacuum level to zero.

To simulate the TaON- and Ta_3N_5-vacuum interfaces, we considered the (001) direction in both cases by building two ($2\vec{a}$ × $1\vec{b}$) slabs (vacuum built along the $\vec{c}$ direction) that contain 6 and 9 atomic layers, respectively. Full slab relaxation was performed by holding the bulk optimized cell parameters constant. For each slab model, the vacuum thickness added to separate each neighboring slab was carefully optimized to avoid any electronic interaction between the two sides of the slab. Moreover, the crystal thickness of each slab was carefully optimized to ensure an accurate reproduction of the band gaps of the bulk materials. A slab thickness of 15 Å and a vacuum thickness of 15 Å allowed a good reproduction of the bulk properties of these materials. The electronic density of states calculations using HSE06 for the two slab models are reported in the Supplementary Information (Figure S1).

To determine the energy of the vacuum level in each slab system, we calculated the electrostatic potential by employing the HSE06 formalism following a methodology described in VASP5.2.[32-35] Dipole corrections were also added to the local potential to correct for any possible error introduced by the periodic boundary conditions. The corresponding profiles of the averaged electrostatic potential over plans parallel to the surface obtained for the two ($2\vec{a}$ × $1\vec{b}$) TaON and pure Ta_3N_5 slabs are reported in the Supplementary Information (Figure S2).

Bulk formation energy calculation

The formation energy of the various explored materials was calculated using NH_3 in the gas phase as nitrogen source.[10,12-15] Depending on the stoichiometry of the modified material, the following three chemical reactions (3-5) were considered:

$$TaON + 2xNH_3 \rightarrow TaO_{(1-3x)}N_{(1+2x)} + 3xH_2O \quad (3)$$

$$(3-x)TaON + (2-4x)NH_3 \rightarrow Ta_{(3-x)}N_{(5-5x)}O_{5x} + (3-6x)H_2O \quad (4)$$

$$3TaON + (2-2x)NH_3 \rightarrow Ta_3N_{(5-2x)}O_{3x} + (3-3x)H_2O \quad (5)$$

For reaction (3), the formation energy was calculated using equation (6):

$$E_{form}(3)=E_{form}^{0K}(3)+[3x.\Delta\mu_{H_2O}-2x.\Delta\mu_{NH_3}] \quad (6)$$

where

$$E_{form}^{0K}(3)=E_{tot}(TaO_{(1-3x)}N_{(1+2x)})-E_{tot}(TaON)+3x.E_{H_2O}-2x.E_{NH_3}$$

Equation (6) shows that $E_{form}(3)$ includes the total energies at 0 K for the TaON, $TaO_{(1-3x)}N_{(1+2x)}$ solids and for isolated H_2O and NH_3 molecules as well as the thermal part of the chemical potentials of water ($\Delta\mu_{H_2O}$) and ammonia ($\Delta\mu_{NH_3}$) that depend on the pressure (*p*) and on the temperature (*T*) through the enthalpy correction (*h*) and entropy (*s*) of each gas phase molecule as follows:

$$\Delta\mu_{H_2O} = h_{H_2O}(T) - Ts_{H_2O}(T) + RTLn(\frac{p(H_2O)}{p_0}) \quad (7)$$

A similar expression holds for $\Delta\mu_{NH_3}$. Based on the experimental conditions, $\Delta\mu_{NH_3}$ was fixed at -1.81 eV for T = 1200 K (typical annealing temperature of Ta_3N_5) at $p(NH_3)$ = 1 atm (standard thermodynamic conditions), respectively.

The zero point vibrational energy, the enthalpy correction (h) and the entropy (s) of each molecule as a function of the temperature (T) were calculated using DMol[45] within the PBE exchange-correlation functional and the DNP basis set.[46] The zero point vibrational energy was systematically included in the enthalpy and entropy corrections. The thermal contributions of the solids were neglected. All electronic energies (for solids and molecules) were calculated with VASP5.2.

In the general case, $\Delta\mu_{H_2O}$ and $\Delta\mu_H$ are expressed as a function of T, $p(H_2O)$ and $p(H_2)$ similarly to equation (7). In the following calculations, $\Delta\mu_H$ was fixed at -1.36 eV for T = 1200 K and $p(H_2) = 10^{-5}$ atm (as the experimental pressure is usually negligible). $\Delta\mu_O$ is variable as a function of $\Delta\mu_{H_2O}$ and can be fixed by changing $p(H_2O)$ using the following equation:

$$\Delta\mu_{H_2O} = \Delta\mu_O + 2\Delta\mu_H \quad (8)$$

Similarly, for reaction (4), the formation energies were normalized by Ta and expressed as follows:

$$E_{form}(4) = E^{0K}_{form}(4) + \frac{1}{(3-x)}[(3-6x).\Delta\mu_{H_2O} - (2-4x).\Delta\mu_{NH_3}] \quad (9)$$

where

$$E^{0K}_{form}(4) = \frac{1}{(3-x)}[E_{tot}(Ta_{(3-x)}N_{(5-5x)}O_{5x}) - (3-x).E_{tot}(TaON) + (3-6x).E_{H_2O} - (2-4x).E_{NH_3}]$$

For reaction (5), the formation energies per Ta were expressed as follows:

$$E_{form}(5) = E^{0K}_{form}(5) + \frac{1}{3}[(3-3x).\Delta\mu_{H_2O} - (2-2x).\Delta\mu_{NH_3}] \quad (10)$$

with

$$E^{0K}_{form}(5) = \frac{1}{3}[E_{tot}(Ta_3N_{(5-2x)}O_{3x}) - 3E_{tot}(TaON) + (3-3x).E_{H_2O} - (2-2x).E_{NH_3}]$$

The formation energy per Ta for pure Ta_3N_5 was calculated using either equation (9) or (10) for x = 0.

Acknowledgements

This work was supported by Award No. UK-C0017, made by King Abdullah University of Science and Technology (KAUST). The authors gratefully thank the High Performance Computing department (HPC) at KAUST for the computational time granted to this work.

Notes and references

[a] Division of Physical Sciences and Engineering, KAUST Catalysis Center (KCC), King Abdullah University of Science and Technology (KAUST), 4700 KAUST, Thuwal 23955-6900, Kingdom of Saudi Arabia, E-mail: moussab.harb@kaust.edu.sa, kazuhiro.takanabe@kaust.edu.sa.

[b] Université de Lyon, CNRS, Ecole Normale Supérieure de Lyon, Laboratoire de Chimie, 46 allée d'Italie, 69364 Lyon cedex 07, France.

[c] IFP Energies Nouvelles, Rond-point de l'échangeur de Solaize, BP 3-69360 Solaize, France.

[d] Department of Chemical System Engineering, The University of Tokyo, 7-3-1 Hongo, Bunkyo-ku, Tokyo, 113-8656, Japan.

† Electronic Supplementary Information (ESI) available: [Electronic density of states and averaged electrostatic potential calculated using the DFT-HSE06 method for TaON and pure Ta_3N_5 slab models. Scanning electron micrographs and X-ray diffraction patterns for the prepared Ta_2O_5, TaON and Ta_3N_5 samples. DFT-optimized metastable structures and relative energies obtained using the DFT-PBE method for $TaO_{0.90}N_{1.06}$ and $Ta_{2.91}N_{4.58}O_{0.41}$ materials. DFT-optimized lowest-energy and metastable structures together with the relative energies (in brackets) and lattice parameters obtained using the DFT-PBE method for $Ta_3N_{4.83}O_{0.25}$ material. Electronic density of states calculated using the DFT-PBE method for bulk TaON and pure Ta_3N_5 materials. Electronic density of states and UV-Vis optical absorption spectrum calculated using the DFT (DFPT)-HSE06 methods for bulk $Ta_3N_{4.83}O_{0.25}$ material. Cyclic voltammograms and Mott-Schottky plots for the prepared TaON and Ta_3N_5 samples. Band edge positions predicted by the DFT-HSE06 method for bulk $Ta_3N_{4.83}O_{0.25}$ material]. See DOI: 10.1039/b000000x/

1. A. J. Esswein and D. G. Nocera, *Chemical Reviews*, 2007, **107**, 4022-4047.
2. K. Maeda and K. Domen, *The Journal of Physical Chemistry C*, 2007, **111**, 7851-7861.
3. A. Kudo and Y. Miseki, *Chemical Society Reviews*, 2009, **38**, 253-278.
4. K. Maeda and K. Domen, *The Journal of Physical Chemistry Letters*, 2010, **1**, 2655-2661.
5. M. G. Walter, E. L. Warren, J. R. McKone, S. W. Boettcher, Q. Mi, E. A. Santori and N. S. Lewis, *Chemical Reviews*, 2010, **110**, 6446-6473.
6. S. Wang and L.-W. Wang, *Physical Review Letters*, 2010, **104**, 065501.
7. S. Venkataraj, D. Severin, S. H. Mohamed, J. Ngaruiya, O. Kappertz and M. Wuttig, *Thin Solid Films*, 2006, **502**, 228-234.
8. Y.-I. Kim, P. M. Woodward, K. Z. Baba-Kishi and C. W. Tai, *Chemistry of Materials*, 2004, **16**, 1267-1276.
9. K. Miga, K. Stanczyk, C. Sayag, D. Brodzki and G. Djéga-Mariadassou, *Journal of Catalysis*, 1999, **183**, 63-68.
10. G. Hitoki, T. Takata, J. N. Kondo, M. Hara, H. Kobayashi and K. Domen, *Chemical Communications*, 2002, 1698-1699.
11. M. Hara, E. Chiba, A. Ishikawa, T. Takata, J. N. Kondo and K. Domen, *The Journal of Physical Chemistry B*, 2003, **107**, 13441-13445.
12. M. Hara, G. Hitoki, T. Takata, J. N. Kondo, H. Kobayashi and K. Domen, *Catalysis Today*, 2003, **78**, 555-560.
13. W.-J. Chun, A. Ishikawa, H. Fujisawa, T. Takata, J. N. Kondo, M. Hara, M. Kawai, Y. Matsumoto and K. Domen, *The Journal of Physical Chemistry B*, 2003, **107**, 1798-1803.
14. E. Orhan, F. Tessier and R. Marchand, *Solid State Sciences*, 2002, **4**, 1071-1076.

15. S. J. Henderson and A. L. Hector, *Journal of Solid State Chemistry*, 2006, **179**, 3518-3524.
16. L. Yuliati, J.-H. Yang, X. Wang, K. Maeda, T. Takata, M. Antonietti and K. Domen, *Journal of Materials Chemistry*, 2010, **20**, 4295-4298.
17. C.-T. Ho, K.-B. Low, R. F. Klie, K. Maeda, K. Domen, R. J. Meyer and P. T. Snee, *The Journal of Physical Chemistry C*, 2010, **115**, 647-652.
18. M. Yashima, Y. Lee and K. Domen, *Chemistry of Materials*, 2007, **19**, 588-593.
19. M. Ritala, P. Kalsi, D. Riihelä, K. Kukli, M. Leskelä and J. Jokinen, *Chemistry of Materials*, 1999, **11**, 1712-1718.
20. E. Nurlaela, S. Ould-Chikh, M. Harb, S. D. Gobbo, M. Aouine, E. Puzenat, P. Sautet, K. Domen, J. M. Basset and K. Takanabe, *Chemistry of Materials*. DOI: 10.1021/cm502015q.
21. C. M. Fang, E. Orhan, G. A. de Wijs, H. T. Hintzen, R. A. de Groot, R. Marchand, J. Y. Saillard and G. de With, *Journal of Materials Chemistry*, 2001, **11**, 1248-1252.
22. C. Stampfl and A. J. Freeman, *Physical Review B*, 2003, **67**, 064108.
23. C. Stampfl and A. J. Freeman, *Physical Review B*, 2005, **71**, 024111.
24. P. Li, W. Fan, Y. Li, H. Sun, X. Cheng, X. Zhao and M. Jiang, *Inorganic Chemistry*, 2010, **49**, 6917-6924.
25. J. Wang, T. Fang, L. Zhang, J. Feng, Z. Li and Z. Zou, *Journal of Catalysis*, 2014, **309**, 291-299.
26. J. Paier, M. Marsman, K. Hummer, G. Kresse, I. C. Gerber and J. G. Ángyán, *The Journal of Chemical Physics*, 2006, **124**, 154709.
27. M. Harb, P. Sautet and P. Raybaud, *The Journal of Physical Chemistry C*, 2011, **115**, 19394-19404.
28. M. Harb, P. Sautet and P. Raybaud, *The Journal of Physical Chemistry C*, 2013, **117**, 8892-8902.
29. M. Harb, *The Journal of Physical Chemistry C*, 2013, **117**, 12942-12948.
30. M. Harb, D. Masih, S. Ould-Chikh, P. Sautet, J.-M. Basset and K. Takanabe, *The Journal of Physical Chemistry C*, 2013, **117**, 17477-17484.
31. M. Harb, *The Journal of Physical Chemistry C*, 2013, **117**, 25229-25235.
32. G. Kresse and J. Hafner, *Physical Review B*, 1994, **49**, 14251-14269.
33. G. Kresse and J. Furthmüller, *Computational Materials Science*, 1996, **6**, 15-50.
34. G. Kresse and J. Furthmüller, *Physical Review B*, 1996, **54**, 11169-11186.
35. G. Kresse and D. Joubert, *Physical Review B*, 1999, **59**, 1758-1775.
36. J. P. Perdew, K. Burke and M. Ernzerhof, *Physical Review Letters*, 1996, **77**, 3865-3868.
37. P. E. Blöchl, *Physical Review B*, 1994, **50**, 17953-17979.
38. H. J. Monkhorst and J. D. Pack, *Physical Review B*, 1976, **13**, 5188-5192.
39. J. Heyd, G. E. Scuseria and M. Ernzerhof, *The Journal of Chemical Physics*, 2003, **118**, 8207-8215.
40. M. Gajdoš, K. Hummer, G. Kresse, J. Furthmüller and F. Bechstedt, *Physical Review B*, 2006, **73**, 045112.
41. M. Launay, F. Boucher and P. Moreau, *Physical Review B*, 2004, **69**, 035101.
42. S. Saha, T. P. Sinha and A. Mookerjee, *Physical Review B*, 2000, **62**, 8828-8834.
43. C. G. Van de Walle and R. M. Martin, *Physical Review B*, 1987, **35**, 8154-8165.
44. A. Franciosi and C. G. Van de Walle, *Surface Science Reports*, 1996, **25**, 1-140.
45. M. R. Hoffmann, S. T. Martin, W. Choi and D. W. Bahnemann, *Chemical Reviews*, 1995, **95**, 69-96.
46. B. Delley, *The Journal of Chemical Physics*, 1990, **92**, 508-517.
47. S. G. Ebbinghaus, H.-P. Abicht, R. Dronskowski, T. Müller, A. Reller and A. Weidenkaff, *Progress in Solid State Chemistry*, 2009, **37**, 173-205.
48. N. S. Alhajri, H. Yoshida, D. H. Anjum, A. T. Garcia-Esparza, J. Kubota, K. Domen and K. Takanabe, *Journal of Materials Chemistry A*, 2013, **1**, 12606-12616.
49. T. Takata, D. Lu and K. Domen, *Crystal Growth & Design*, 2010, **11**, 33-38.
50. A. Dabirian, H. v. t. Spijker and R. van de Krol, *Energy Procedia*, 2012, **22**, 15-22.
51. A. Dabirian and R. van de Krol, *Applied Physics Letters*, 2013, **102**, 033905.
52. A. L. Linsebigler, G. Lu and J. T. Yates, *Chemical Reviews*, 1995, **95**, 735-758.
53. Y. Cong, H. S. Park, H. X. Dang, F.-R. F. Fan, A. J. Bard and C. B. Mullins, *Chemistry of Materials*, 2012, **24**, 579-586.
54. K. Reuter and M. Scheffler, *Physical Review B*, 2001, **65**, 035406.
55. K. Reuter and M. Scheffler, *Physical Review B*, 2003**, 68,** 045407.